

A Hybrid PWM Technique Employing Variable Switching Sequences for Current Ripple Suppression in Dual Three-Phase PMSMs

Sunbo Wang^{ID}, Marco Rivera^{ID}, *Senior Member, IEEE*, Dmitry Golovanov^{ID}, Jonathan Blissett, Jonathan Moran, Paul Davison, G. Ramtharan, Chris Gerada^{ID}, *Senior Member, IEEE*, and Patrick Wheeler^{ID}, *Fellow, IEEE*

Abstract—Dual three-phase electrical machines inherently have lower $6k \pm 1$ order harmonic impedance than conventional three-phase machines, particularly in their sensitivity to voltage pulses from a drive in terms of current harmonics. Based on space vector pulse width modulation (SVPWM) methods, this article introduces a systematic approach to numerate all the feasible switching sequences and examine their current harmonic performance. Five distinct switching sequences, along with their optimal operational regions determined by modulation vector position, are proposed, considering variations in the machine parameters. A straightforward PWM generation method, incorporating dead-time compensation, is also considered. The theoretical evaluation has been validated with both piecewise linear electrical circuit simulation (PLECS) simulation results and experimental evaluation conducted on a 270 kW hardware prototype.

Index Terms—Asymmetrical dual three-phase PMSM, current ripple suppression, multiphase drives, space vector pulse width modulation (SVPWM).

Received 24 June 2024; revised 7 September 2024; accepted 2 October 2024. This work was supported by Agencia Nacional de Investigación y Desarrollo (ANID) FONDECYT Regular under Grant 1220556, ANID under Grant FOVI230169, Fondap SERC under Grant 1523A0006, the Research Project PINV01-743 of the Consejo Nacional de Ciencia y Tecnología (CONACYT), ENNOBLE-R02401, and IRCF project from the University of Nottingham under Grant 24932270. (Corresponding author: Sunbo Wang.)

Sunbo Wang, Chris Gerada, and Patrick Wheeler are with the Department of Electrical and Electronic Engineering, Faculty of Engineering, Power Electronics, Machines and Control (PEMC) Research Institute, University of Nottingham, NG7 2GT Nottingham, U.K. (e-mail: sunbo.wang@nottingham.ac.uk; eezcg@exmail.nottingham.ac.uk; pat.wheeler@nottingham.ac.uk).

Dmitry Golovanov, Jonathan Blissett, Jonathan Moran, Paul Davison, and G. Ramtharan are with Fortescue Zero Ltd., Unit 5 Technology, OX5 1GN Kidlington, U.K. (e-mail: dmitry.golovanov@wae.com; jon.blissett@wae.com; jonathan.moran@wae.com; paul.davison@wae.com; ram.pillai@wae.com).

Marco Rivera is with the Department of Electrical and Electronic Engineering, Faculty of Engineering, Power Electronics, Machines and Control (PEMC) Research Institute, University of Nottingham, NG7 2GT Nottingham, U.K., and also with the Laboratorio de Conversión de Energías y Electrónica de Potencia (LCEEP), Vicerrectoría Académica, Universidad de Talca, Talca 3460000, Chile (e-mail: Marco.Rivera@nottingham.ac.uk; marcoriv@utalca.cl).

Digital Object Identifier 10.1109/TIE.2024.3476911

I. INTRODUCTION

BENEFITING from the advantages of low torque ripple and a good fault-tolerant capability, as well as low power rating drive system-phase, multiphase machines have been widely used in applications requiring high reliability and high-power density [1], [2].

Dual three-phase permanent magnet synchronous machines (DTP-PMSM) are popular among multiphase motors due to their simple structure. The DTP-PMSM usually has two sets of balanced three-phase winding spatially shifted by 30 electrical degrees with insulated neutral points, which can be driven by two individual three-phase voltage source inverters [3].

Compared with the conventional three-phase PMSM, the DTP-PMSM has a drawback of the lower $6k \pm 1$ ($k = 1, 3, 5 \dots$) order harmonic impedance, and a small voltage harmonic can generate large current harmonics [4]. These harmonics can be mapped on the z_1 - z_2 subspace according to the vector-space decomposed theory, which is not associated with electromechanical energy transfer but can result in extra copper loss [5]. Besides, the current harmonics from pulse width modulation effects can also lead to additional motor iron loss as well as vibration and noise [6], [7].

To improve efficiency and increase the life of the machine, some research has been presented to address the current harmonics problems in DTP-PMSM drive systems. Previous current harmonics suppression strategies can be classified into two categories. The first one minimizes low-frequency current harmonics with current harmonic regulators. Proportional-integral controllers, proportional-resonant controllers or disturbance observer have been used to eliminate seventh current harmonics in the z_1 - z_2 subspace [8], [10], [11], [12], [13], [14]. Current harmonics with various orders can also be extracted using virtual multithree-phase systems and suppressed separately [9]. However, these methods are based on a three-phase inverter's average model, can only suppress low-frequency current harmonics. Thus, high-frequency voltage harmonics from differential pulses between two sets of windings can still produce significant current harmonics [16].

Other current harmonics suppression strategies are based on the optimized pulse width modulation (PWM), including carrier-based PWM (CPWM) and space-vector PWM (SVPWM), which is aimed to suppress switching current harmonics. CPWM

modulation encompasses techniques such as sine-triangle PWM, single zero-sequence injection PWM (SZIPWM) [15], and double zero-sequence injection PWM (DZIPWM) which offers the lowest harmonic distortion and optimal dc-bus utilization [16]. SVPWM, through its application of vector decomposition theory, enables a detailed analytical evaluation of current harmonic performance compared with CPWM [17]. The key desired feature of SVPWM is synthesizing space vectors in a switching period to represent reference average voltage in the α - β subspace, which requires a minimum of five distinct space vectors, four of which are active [18]. The four largest space vectors are adopted with the consideration of reference voltage in α - β subspace and z_1 - z_2 subspace [5], [18]. A switching sequence optimization approach with the four largest space vectors is proposed based on circulating current predictions [25]. Simplifications were introduced in the 24-sector SVPWM by replacing one largest space vector with one base vector [19], or two base space vectors [20]. This 24-sector SVPWM can be merged with other methods such as discontinuous SVPWM [19], overmodulation [21], and synchronized SVPWM [22], [23]. Unfortunately, 24-sector SVPWM underperforms in current ripple suppression compared with 12-sector SVPWM when the modulation vector amplitude is high [19]. Viewing 24-sector SVPWM as a two three-phase frame-based method, the hybrid PWM strategy which can fully utilize the current ripple suppression characteristics of 24-vector SVPWM is proposed [26]. However, certain PWM techniques with good current ripple performance [5], [18] are excluded from this hybrid approach due to switching constraints. These limitations restrict a fully generalized discussion of all possibilities.

Consideration has been given to enumerating possible PWM switching sequences and evaluating their performance under different conditions. However, it is difficult due to the complexity of the selection and arrangement of space vectors in switching sequences. To solve this problem, a systematic approach is introduced to explore all feasible switching sequences. This approach uses a finite switching sequences model to swiftly evaluate the capability of the PWM strategy to mitigate switching current harmonics. Among a vast array of possibilities, five switching sequences showing promise in current ripple suppression are identified, including two sequences that are different from existing methodologies. The optimal operational regions for each sequence are determined according to the modulation vector, which is integrated into a hybrid optimal PWM technique. This approach capitalizes on the synergistic benefits of combining the optimal regions of various sequences, thereby optimizing overall performance across the entire operational range. The variation of machine parameters is accounted for in the proposed PWM technique. Furthermore, a straightforward carrier-based mechanism, augmented with dead-time compensation, is devised to produce the intricate PWM waveform. Simulation and experiment results are given to verify the performance of the proposed PWM technique.

II. CURRENT RIPPLE MODEL WITH FINITE SWITCHING SEQUENCES

The power circuit of the two-level dual three-phase machine drive is shown in Fig. 1, which includes two three-phase inverters, inverter-I and inverter-II sharing the same dc bus. There are 64

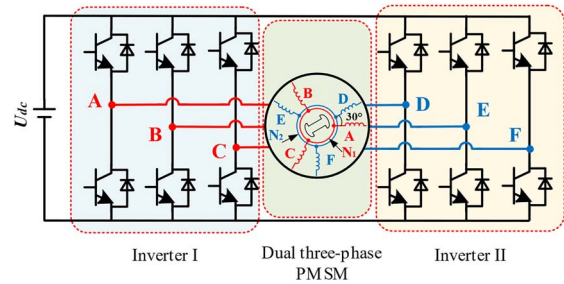


Fig. 1. Power circuit of dual three-phase machine drive.

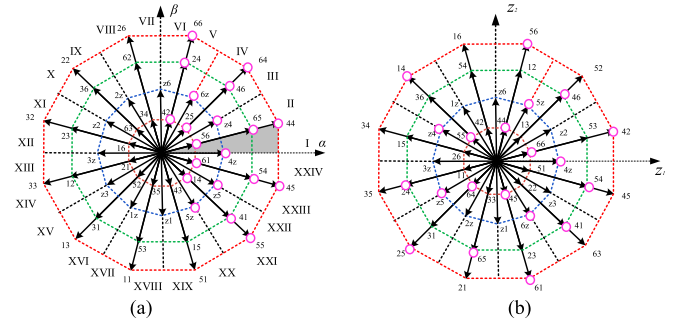


Fig. 2. 64-space vectors of the dual three-phase drive, and mapping of the 24 adjacent switching states to sector-I. (a) α - β subspace. (b) z_1 - z_2 subspace.

switching states for the dual three-phase voltage source inverter. Each switching state is represented by a binary number ($S_a, S_b, S_c, S_d, S_e, S_f$), which gives the state of the upper switches. The $S = 1$ and $S = 0$ denote the “on” and “off” states, respectively. The 64 switching states can be described by octal numbers with order as ($S_a S_b S_c, S_d S_e S_f$). Based on the vector decomposition theory, the space vectors can be mapped by the matrix given in (1) and (2) into three subspaces, as α - β , z_1 - z_2 and o_1 - o_2 [5]. The components of the voltage vectors on the α - β and z_1 - z_2 subspace are shown in Fig. 2. The 4-D space vectors include four zero vectors ($v_{00}, v_{07}, v_{70}, v_{77}$), 60 active vectors which are categorized into large vectors v_L , medium vectors v_M , base vectors v_B , and small vectors v_S . The α - β subspace is divided into 24 sectors by v_L . The modulation in each sector can be analyzed with the help of 24 adjacent space vectors in α - β subspace, as shown in Fig. 2 for sector I. In Fig. 2, z represents the zero-state as $z \in \{0,7\}$

$$\begin{aligned}
 & [F_\alpha \ F_\beta \ F_{z1} \ F_{z2} \ F_{o1} \ F_{o2}]^T \\
 &= [T_6] \cdot [F_a \ F_b \ F_c \ F_d \ F_e \ F_f]^T \\
 & [T_6] = \frac{1}{3} \begin{bmatrix} 1 & -1/2 & -1/2 & \sqrt{3}/2 & -\sqrt{3}/2 & 0 \\ 0 & \sqrt{3}/2 & -\sqrt{3}/2 & 1/2 & 1/2 & -1 \\ 1 & -1/2 & -1/2 & -\sqrt{3}/2 & \sqrt{3}/2 & 0 \\ 0 & -\sqrt{3}/2 & \sqrt{3}/2 & 1/2 & 1/2 & -1 \\ 1 & 1 & 1 & 0 & 0 & 0 \\ 0 & 0 & 0 & 1 & 1 & 1 \end{bmatrix}.
 \end{aligned} \tag{1}$$

For the dual three-phase inverter, the goal of the SVPWM or CPWM is to generate the fundamental component of the

reference voltage in the α - β subspace for power conversion, and simultaneously preserve zero average voltage in the z_1 - z_2 subspace to prevent unwanted current harmonics and additional loss. Assuming a switching sequence with J switching states as $\{v_1, v_2, v_3, \dots, v_j\}$ is adopted in the per-carrier period, The following equations are satisfied:

$$\begin{cases} V_\alpha^* = \sum_{j=1}^J v_{\alpha j} T_j, & V_\beta^* = \sum_{j=1}^J v_{\beta j} T_j \\ V_{z1}^* = \sum_{j=1}^J v_{z1j} T_j, & V_{z2}^* = \sum_{j=1}^J v_{z2j} T_j \\ T_{sw} = \sum_{j=1}^J T_j \end{cases} \quad (2)$$

where V_α^* , V_β^* , V_{z1}^* , and V_{z2}^* are the reference voltage in the α - β and z_1 - z_2 subspace, respectively. v_α , v_β , v_{z1} , and v_{z2} are the normalized projection of v_j onto the α - β and z_1 - z_2 subspace, T_j is the active time of j th switching states, T_{sw} is the time for one PWM period. According to [19], the voltage, current and stator flux can be separated into harmonic components. Assuming the fundamental components remain constant over the per-carrier period, the harmonic voltage equation can be expressed as

$$\begin{aligned} \Delta v_{s\alpha\beta} &= \frac{d\Delta\lambda_{s\alpha\beta}}{dt} \\ \Delta v_{sz12} &= \frac{d\Delta\lambda_{sz12}}{dt} \end{aligned} \quad (3)$$

where Δv_s and $\Delta\lambda_s$ are the ripple components of the voltage and stator flux. Δv_s can be calculated by the difference between the actual switching states v_j and the reference voltages V^* as

$$\begin{aligned} \Delta v_{s\alpha\beta} &= [v_{j\alpha} - V_\alpha^* \quad v_{j\beta} - V_\beta^*]^T \\ \Delta v_{sz12} &= [v_{z1} - V_{z1}^* \quad v_{z2} - V_{z2}^*]^T. \end{aligned} \quad (4)$$

Since the average stator flux ripple over the per-carrier period is zero, the current ripple components are zero at the beginning and the end. The value of the stator flux ripple component in α - β and z_1 - z_2 subspace after j th switching states can be obtained by integrating the voltage ripple with time

$$\begin{aligned} \Delta\lambda_{\alpha\beta}|_j &= \Delta v_{s\alpha\beta}|_j \cdot T_j + \Delta\lambda_{\alpha\beta}|_{j-1} \\ \Delta\lambda_z|_j &= \Delta v_{sz}|_j \cdot T_j + \Delta\lambda_z|_{j-1}. \end{aligned} \quad (5)$$

Based on (5), the RMS stator flux ripple can also be calculated as

$$\Delta\lambda_{rms} = \sqrt{\int_{NT_s}^{(N+1)T_s} \Delta\lambda^2 dt} = \sqrt{\frac{1}{3} \sum_{j=1}^J (\Delta\lambda_{j-1}^2 + \Delta\lambda_{j-1} \Delta\lambda_j + \Delta\lambda_j^2)}. \quad (6)$$

From (6), the rms current ripple Δi_{rms} is expressed as $\Delta i_{rms} = \Delta\lambda_{rms}/L_s$, which can represent components in the α , β , z_1 , or z_2 axis.

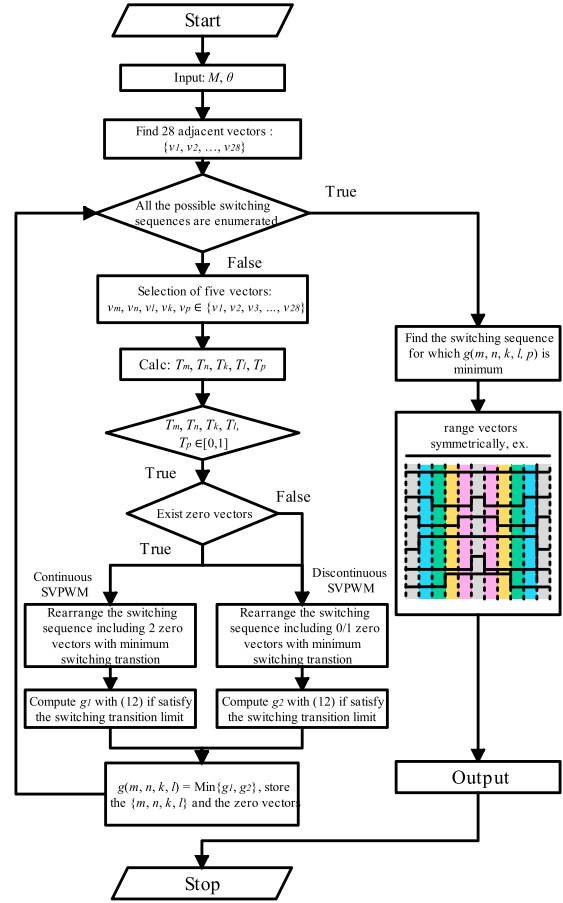


Fig. 3. Flow diagram of the proposed SVPWM optimization strategy under modulation point (M, θ) .

III. FINITE SWITCHING SEQUENCES BASED SVPWM OPTIMIZATION STRATEGY

A. Basic Principle

The proposed SVPWM strategy offers an optimization framework aimed at optimal switching sequences to reduce current ripple components. After acknowledging machine parameters, specifying the number of switching states, and modulation vector for one PWM period, all the admissible switching sequences can synthesize the reference voltage in α - β and z_1 - z_2 subspace are enumerated, and the corresponding time for each switching state is obtained. Considering the placement and selection of zero switching states existing in the switching sequences, the modulation performance can be predicted during the whole PWM period. Then, the optimization objective is designed to evaluate the current ripple performance of each switching sequence, and the one that yields the minimal current ripple is sorted out. The optimal PWM waveform can be generated after distributing each vector symmetrically in the PWM cycle as Fig. 3. This optimization approach can be repeated for different modulation vectors, and optimized switching sequences for the whole modulation region can be solved numerically. The modulation vector is quantized with modulation amplitude ration as $M = \sqrt{V_\alpha^2 + V_\beta^2}/V_{dc}$ and modulation angle θ . The flow

TABLE I
OPTIMAL SWITCHING SEQUENCES FOR PROPOSED HYBRID
SVPWM STRATEGY

Category	Name	Optimal Switching Sequence Over $T_s/2$	Vector Types	k_f
Group 1	Seq1	07 – 05 – 45 – 44 – 64 – 70	$3v_L + 1v_B + 2v_Z$	1
Group 2	Seq2	70 – 64 – 44 – 45 – 55	$4v_L + 1v_Z$	6/5
Group 3	Seq3	07 – 05 – 45 – 44 – 64	$3v_L + 1v_B + 1v_Z$	3/2
	Seq4	55 – 45 – 44 – 64 – 60	$4v_L + 1v_B$	3/2
	Seq5	55 – 45 – 44 – 64 – 66	$5v_L$	3/2

diagram of the proposed SVPWM optimization strategy is shown in Fig. 3.

B. Optimization Objective

The current waveform quality of the PWM drives is mainly determined by the switching frequency harmonics, which contribute significantly to the current harmonic distortion (THD) and the torque ripple. Reflecting on the form of THD, the current harmonic components from the PWM effect can be described as the total rms value of the current ripple component in the six-phase, as well as the α , β , z_1 , or z_2 axis, which can be calculated from (6)

$$\begin{aligned} \Delta i_{\text{rms}} &= \sqrt{\sum \Delta i_{j,\text{rms}}^2} \\ &= \frac{1}{L_{\alpha\beta}} \sqrt{\Delta \lambda_{\alpha\text{rms}}^2 + \Delta \lambda_{\beta\text{rms}}^2 + \mu^2(\Delta \lambda_{z_1\text{rms}}^2 + \Delta \lambda_{z_2\text{rms}}^2)} \quad (7) \end{aligned}$$

where Δi_{rms} is the total rms value of the current ripple components from the PWM effect, $\Delta i_{j,\text{rms}}$ is the rms value of the current ripple in the j th phase, $L_{\alpha\beta}$ is the stator inductance on $\alpha\beta$ -subspace and μ is the ratio between $\alpha\beta$ and z_1 - z_2 subspace inductance which is defined as $\mu = L_{\alpha\beta}/L_{z_1z_2}$.

Evaluating the performance of various switching sequences requires a consistent framework for comparison, especially regarding the number of switching transitions. The goal of this comparative analysis is to maintain uniform switching efforts across different switching sequences, which is assessed by ensuring a consistent average switching frequency. The average switching frequency computation method counts the total number of switching transitions over one line-cycle and obtains the average value. Since the dual three-phase inverters consist of 12 switching, the average switching frequency can be written as [25]

$$f_{\text{sw}} = \frac{1}{12 \cdot 2NT_s} \sum_{n=1, i=a \sim z}^N |S_i(n) - S_i(n-1)| \quad (8)$$

where N denotes the number of switching states in one line-cycle, and T_s is the PWM carrier period time. A factor k_f defined as the ratio between the PWM carrier frequency (f_s) and the average switching frequency (f_{sw}), i.e., $k_f = f_s/f_{\text{sw}}$, is calculated from (8) and summarized in Table I. By ensuring a uniform average switching frequency across various sequences, the optimization

objective is established based on (9) as

$$g = \frac{1}{L_{\alpha\beta}k_f} \sqrt{\Delta \lambda_{\alpha\text{rms}}^2 + \Delta \lambda_{\beta\text{rms}}^2 + \mu^2(\Delta \lambda_{z_1\text{rms}}^2 + \Delta \lambda_{z_2\text{rms}}^2)}. \quad (9)$$

It can be shown that μ is the sole machine parameter prerequisite for knowledge when comparing the current ripple performance between different switching sequences.

C. Pulse Pattern Selection Criterion

There are infinite possible switching sequences for each PWM period if no criteria or rules are adopted for the switching states arrangement and selection. To diminish the number of admissible switching sequences to finite, the number of switching states, the range of switching states involved, and the placement and choice of zero switching states need to be decided before implementing the optimization strategy shown in Fig. 3. The design criteria are listed as follows.

- 1) *Number of switching states*: mathematically, there are a maximum of six vectors required for synthesizing reference voltage as well as minimizing current ripple. All the PWM strategies in [5], [18], [19], [20], [21], [22], [23], [24], [25], [26] involve five active vectors or four active vectors in their switching sequence, with zero space vectors as a supplement for reference voltage synthesis. To avoid excessive computational overhead, a sequence consisting of five space vectors is chosen, which makes it possible to explore both continuous and discontinuous conditions by the role of existing zero vectors. Switching sequence as $\{v_m, v_n, v_l, v_k, v_p\}$ including at least four active space vectors is adopted to describe the possible case and calculate the corresponding active times.
- 2) *Space vectors involved*: only space vectors adjacent to the reference voltage in the $\alpha\beta$ subspace should be involved in switching sequence optimization in case additional current ripple from less zero vectors active time and more nonzero space vectors in z_1 - z_2 subspace. Therefore, only 24 space vectors including four zero vectors adjacent to the operation sector are considered for optimization. Taking sector-I as an example, all 24 space vectors are mapped in Fig. 2.
- 3) *The placement and selection of zero vectors*: for the switching sequences including zero space vectors, the modulation method can be further classified into continuous SVPWM, with two zero vectors sharing the same time, and discontinuous SVPWM, with only one zero space vector or without zero space vector [5], [18], [19], [20], [21], [22], [23], [24], [25], [26]. Both these approaches are considered in the SVPWM optimization strategy. Taking the case as v_p is zero vectors for example, the switching sequences with zero vectors is $\{v_{z-I}, v_m, v_n, v_l, v_k, v_{z-II}\}$ for the discontinuous SVPWM and $\{v_{z-I}, v_m, v_n, v_l, v_k\}$ or $\{v_m, v_n, v_l, v_k, v_{z-II}\}$ for the continuous SVPWM. The selection of v_{z-I} and v_{z-II} among $\{v_{00}, v_{07}, v_{70}, v_{77}\}$ should minimize the switching transitions from zero vectors to active vectors, which can be

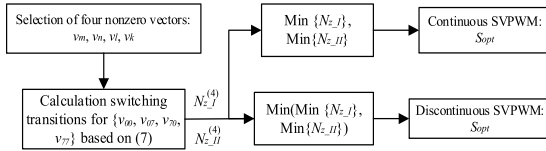


Fig. 4. Principle of zero vectors selection in proposed SVPWM optimization strategy for potential optimal switching sequence.

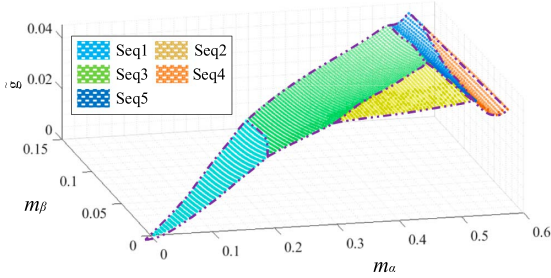


Fig. 5. 15 degrees region-wise hybrid optimal SVPWM techniques and corresponding per-unitized optimization objective g when machine parameter $\mu = 4$.

expressed as

$$\begin{cases} N_{z_I} = \sum_{i=a,b,c,x,y,z} |S_{iz_I} - S_{im}| \\ N_{z_II} = \sum_{i=a,b,c,x,y,z} |S_{iz_II} - S_{ik}| \end{cases} \quad (10)$$

The principle of zero vector selection in the proposed SVPWM optimization strategy for the potential optimal switching sequence is shown in Fig. 4.

IV. PROPOSED HYBRID OPTIMAL SVPWM TECHNIQUES

A. Proposed Hybrid Optimal SVPWM

Utilizing the proposed SVPWM optimization strategy enables the identification of the optimal switching sequence that achieves the best current ripple performance for specified modulation vectors (M, θ) and the machine parameter μ . The optimization algorithm explores the modulation vector space (M, θ) across the entire desirable modulation area, facilitating the numerical determination of the optimal SVPWM techniques. Although the optimization approach can be applied beyond the linear modulation range, overmodulation typically results in the largest space vectors dominating most of the time, reducing the flexibility in selecting switching sequences [21]. Therefore, the discussion is confined to the linear modulation range. Analysis of the results reveals that the modulation regions exhibit symmetry at intervals of 15 degrees. Consequently, the discussion is narrowed to only optimal switching sequences within each 15-degree region. Fig. 5 illustrates the optimal region for varying switching sequences, which takes machine parameter of $\mu = 4$ as an example. The m_α and m_β represent the modulation amplitude ratio in the α axis and β axis respectively, which are defined as $m_{\alpha,\beta} = V_{\alpha,\beta}^*/V_{dc}$. The corresponding optimization objective g is also shown in Fig. 5, which is per-unitized by the base current $V_{dc}T_{sw}/2L_{\alpha\beta}$. Despite the extensive range of possible switching sequences, only five are

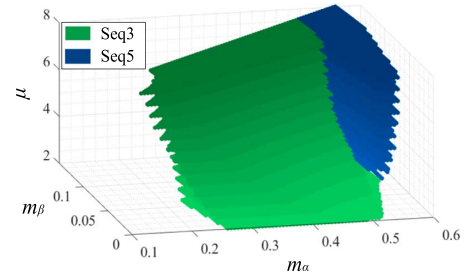


Fig. 6. Optimal regions of Seq3 and Seq5 under various machine parameter μ .

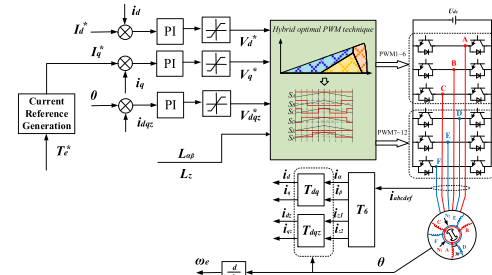


Fig. 7. Control block diagram of the proposed hybrid SVPWM controlled DTP-PMSM drive system.

implemented across various modulation regions for optimal SVPWM techniques. These sequences are identified as optimal and listed in Table I. Specifically, Seq1 in Group-I can be classified into the continuous 24-sector SVPWM as discussed [19], and Seq2 in Group-II aligns with the optimal vector sequences for the 12-sector SVPWM described [5]. Moreover, Seq3 in Group-III is identified as the discontinuous 24-sector SVPWM, also mentioned [19]. However, this analysis illustrates that unlike prior approaches focusing solely on optimizing current ripple performance based on the modulation vector amplitude as reported [5], [18], [19], [20], [21], [22], [23], [24], [25], considering variations in the electric angle alongside the modulation amplitude can further enhance current ripple performance. It is observed that as the modulation amplitude increases, two additional optimal switching sequences, Seq4 and Seq5, emerge as the optimal switching sequences. These sequences, unlike those proposed in earlier studies, are uniquely suited for application in regions of high modulation range, showing significant improvements in current ripple performance. Such improvement is benefited from both the higher k_f and more active time of the largest space vectors v_l .

To generalize the proposed hybrid optimal PWM techniques, the optimal region for different switching sequences is scattered across various machine parameters μ , as depicted in Fig. 6. It is observed from Fig. 5 that the optimal regions for Seq3 and Seq5 delineate all the boundaries between different regions, which are explicitly scattered in Fig. 6. It is noteworthy that as μ increases, the optimal region for Seq1 diminishes, whereas other switching sequences, characterized by a higher carrier frequency ratio k_f , encompass a broader region. The expansion of the optimal regions for Seq2 and Seq5 with an increase in μ is attributed to both sequences incorporating more large space vectors v_l . These vectors possess the smallest magnitude on the z_1z_2 -subspace and

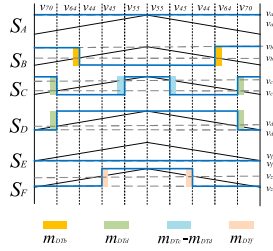


Fig. 8. PWM waveform of Seq2 with carrier-based implementation and dead-time compensation.

introduce the minimum $6k \pm 1$ order current harmonics among active space vectors.

The control block diagram for the proposed hybrid PWM technique applied to DTP-PMSM is depicted in Fig. 7, comprising four current closed loops and a look-up table for deriving current references from torque references. Rotation frames are utilized for both the dq and z_{12} axis currents, with PI regulators applied to each. Under maximum torque per ampere (MTPA) conditions, the d -axis current reference is set to zero in the prototype, and z_{12} axis currents are also zeroed since the z_1z_2 -subspace does not contribute to electromagnetic power conversion. From the average model theory, the PWM technique does not affect PI parameters design by adeptly synthesizing dqz voltage. After several trials, the PI parameters for dq currents were established at $K_p = 1.5$ and $K_i = 100$, while for z_{12} currents, $K_p = 0.8$ and $K_i = 100$ were selected. The dqz inductances help to define the switching sequences' adoption region boundaries. The final PWM output is produced using a carrier-based method.

B. FPGA Implementation

Based on SVPWM theory, calculating the active time for each space vector and generating the corresponding pulse for each phase involves a significant computational burden. One possible approach to avoid that is to generate the PWM waveforms by carrier and duty-ratios, as shown in Fig. 8. Table I reveals that Seq2 in Group 2 represents the most complex implementation challenge, with other sequences being its special cases. Thus, Seq2 serves as the basis for discussing the FPGA implementation of all proposed switching sequences.

First, the duty ratio of each phase can be calculated as

$$\begin{cases} m_a = m_x + m_{z1} \\ m_b = -\frac{1}{2}m_x + \frac{\sqrt{3}}{2}m_\beta - \frac{1}{2}m_{z1} - \frac{\sqrt{3}}{2}m_{z2} \\ m_c = -\frac{1}{2}m_x - \frac{\sqrt{3}}{2}m_\beta - \frac{1}{2}m_{z1} + \frac{\sqrt{3}}{2}m_{z2} \\ m_d = \frac{\sqrt{3}}{2}m_x + \frac{1}{2}m_\beta - \frac{\sqrt{3}}{2}m_{z1} + \frac{1}{2}m_{z2} \\ m_e = -\frac{\sqrt{3}}{2}m_x + \frac{1}{2}m_\beta + \frac{\sqrt{3}}{2}m_{z1} + \frac{1}{2}m_{z2} \\ m_f = -m_\beta - m_{z2} \end{cases} \quad (11)$$

where m_x , m_β , m_{z1} , and m_{z2} represent the duty cycles derived from the dqz voltage reference and dc voltage under a stationary frame. A possible carrier-based PWM generation approach, illustrated in Fig. 8, employs two carriers phased 180 degrees apart for abc and def phases. Two modulation signals, v_1 and v_2 ,

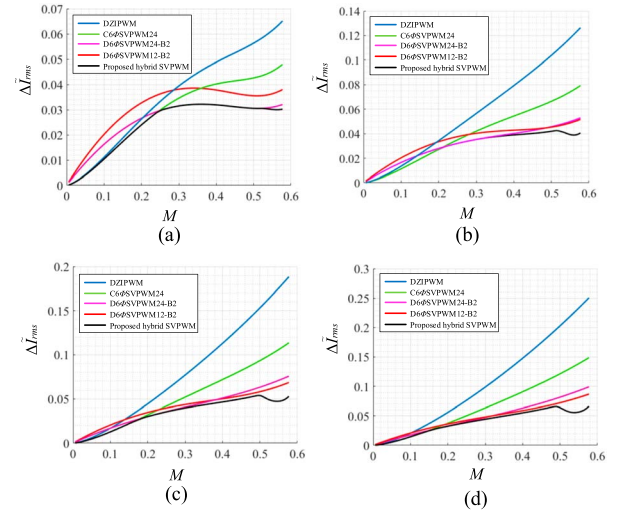


Fig. 9. Comparison of the existing PWM strategies and proposed optimal hybrid SVPWM technique versus modulation amplitude ratio M . (a) $\mu = 2$. (b) $\mu = 4$. (c) $\mu = 6$. (d) $\mu = 8$.

are used to create a symmetrical PWM waveform with multiple pulses per period. The gate signal for the top switch S_k , where $k \in \{a, b, c, d, e, f\}$, is turned off when the carrier is between v_1 and v_2 . The modulation signals can be deduced as

$$\begin{cases} v_{a1} = m_a + 1 - m_{\max 1}, & v_{a2} = 1 \\ v_{b1} = m_b + 1 - m_{\max 1} & v_{b2} = 1 \\ v_{c1} = m_d - v_{\min 2}, & v_{c2} = -m_c + m_{\max 1} + v_{c1} \\ v_{d1} = 0, & v_{d2} = m_d - m_{\min 2} \\ v_{e1} = 0, & v_{e2} = m_e - m_{\min 2} \\ v_{f1} = 0, & v_{f2} = m_f - m_{\min 2} \end{cases} \quad (12)$$

The dead times are compensated to the duty ratio before generation modulation signals. Given the potential for multiple pulses per phase, the compensation ratio of the phase k is deduced as

$$m_{DTk} = 2N \operatorname{sgn}(i_k) \frac{t_{\text{dead}}}{T_s} \quad (13)$$

where t_{dead} is the dead time of dual-three phase inverter, $\operatorname{sgn}(i_k)$ is the current direction of phase k , and N is the number of modulation signals in phase k not equal to 1 or 0. Fig. 8 also demonstrates that dead time compensation does not influence the final space vectors applied to the drive system.

C. Performance Evaluation and Comparison

The proposed hybrid SVPWM technique is compared in Fig. 9 with existing SVPWM and CPWM strategies. The line-cycle rms of the current ripple can be obtained as (14) according to [19]

$$\Delta \tilde{i}_{\text{rms}}(M) = \sqrt{\int_0^{2\pi} \Delta \tilde{i}_{\text{rms}}^2(M, \theta) d\theta} \quad (14)$$

$\Delta \tilde{i}_{\text{rms}}$ is per-unitized of cost function representing per-carrier period current ripple in (7) with respect to base current $V_{\text{dc}}T_{\text{sw}}/2L_{\alpha\beta}$. For comparison purposes, the current ripple performance has been evaluated at the same average switching frequency f_{sw}

TABLE II
PEAK-PEAK VALUE OF COMMON-MODE VOLTAGE NOISE WITH DIFFERENT PWM TECHNIQUES

DZIPWM	Seq1	Seq2	Seq3	Seq4	Seq5
V_{dc}	$V_{dc}/3$	$V_{dc}/3$	$V_{dc}/3$	$V_{dc}/3$	$V_{dc}/3$

for all PWM strategies, which is satisfied with the sampling frequency ratio k_f in (10).

To better evaluate the current ripple performance of proposed hybrid SVPWM techniques, four existing SVPWM strategies are selected, 1) DZIPWM, as a based modulation technique with the best current harmonic performance among CPWM techniques, $k_f = 1$. 2) D6 Φ SVPWM12-B2, one type of discontinuous 12-sector SVPWM strategies [5] with the best current ripple performance, $k_f = 6/5$. 3) Continuous and discontinuous 24-sector SVPWM strategies, as C6 Φ SVPWM24 and D6 Φ SVPWM24-B2, with best current ripple performance among [19], [20], [21], [22], [23], [24], $k_f = 1$ and $k_f = 3/2$, respectively.

The comparison results, computed numerically for a set of fixed machine parameters $\mu = \{2, 4, 6, 8\}$, are displayed in Fig. 9. This figure illustrates that the proposed hybrid optimal PWM technique achieves the lowest rms of the current ripple across all evaluated techniques within the entire range of modulation indices and under varying machine parameters. This outcome illustrates the superior current ripple suppression capability of the proposed PWM strategy.

An analysis combining the insights from Figs. 6 and 9 reveals that for lower values of the machine parameter μ , Seq1 and Seq3 are predominantly utilized, aligning the proposed PWM technique with the curve offering the best current ripple suppression among C6 Φ SVPWM24 and D6 Φ SVPWM24-B2. As the machine parameter μ increases, Fig. 6 indicates that Seq2 and Seq3 are applied together in the middle modulation region, enhancing the current ripple performance of the proposed technique beyond what either sequence could achieve independently. In the upper modulation range, the introduction of switching sequences, Seq4 and Seq5, marks a significant enhancement in current ripple performance against existing PWM methods, particularly for higher μ values. Taking the case $\mu = 4$ for example, the proposed hybrid SVPWM technique can reduce current ripple rms up to 75.4% compared with DZIPWM, 62.3% compared with C6 Φ SVPWM24, 39.3% compared with D6 Φ SVPWM24-B2 and 22.7% compared with D6 Φ SVPWM12-B2.

The average rms value of current ripple, indicative of the switching current harmonic components, represents the differential-mode noise from the PWM effect. In contrast, common-mode voltage noise is another crucial factor in assessing electromagnetic interference (EMI) performance. The common-mode voltage in the DTP-PMSM drive system can be defined as

$$V_{CM} = \frac{1}{6}(V_{AO} + V_{BO} + V_{CO} + V_{DO} + V_{EO} + V_{FO}) \quad (15)$$

where V_{iO} is the phase i output voltage to the center point of dc-bus. The peak-peak value of common-mode voltage across different switching sequences is compared as Table II. Due to the implementation of two zero space vectors v_{00} and v_{77} , the

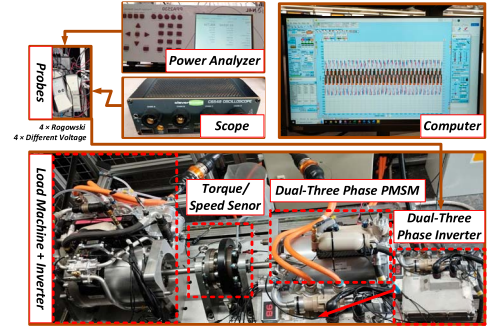


Fig. 10. Experimental setup of the prototype DTP-PMSM.

TABLE III
PARAMETERS OF THE PROTOTYPE DUAL THREE-PHASE PMSM

Parameters	Values
Number of poles	10
Number of slots	12
PM flux linkage (Wb)	0.0477
α - β subspace inductance, $L_{\alpha\beta}$ (μ H)	102
z_1 - z_2 subspace inductance, L_{z1z2} (μ H)	23
M	4.434
Phase resistance ($m\Omega$)	11.6

DZIPWM exhibits the largest peak-to-peak value of common-mode voltage noise. According to aforementioned analysis, the C6 Φ SVPWM24 and Seq1, D6 Φ SVPWM12-B2 and Seq2, D6 Φ SVPWM24-B2 and Seq3 share the same peak-peak value of common-mode noise. These PWM techniques show improved performance in managing common-mode voltage noise compared with the DZIPWM, primarily due to the exclusion of v_{00} or v_{77} from their switching sequences. Despite variations in switching sequences, the proposed hybrid PWM technique maintains a consistent performance in terms of peak-to-peak values of common-mode voltage noise, aligning uniformly with the performance of other existing PWM techniques.

V. SIMULATION AND EXPERIMENTAL RESULTS

To validate the effectiveness of proposed SVPWM strategy, experiments have been performed using the test bench shown in Fig. 10. The 12/10 DTP-PMSM and a dual three-phase 2 level VSI are mechanically coupled. The parameters of the dual three-phase PMSM are shown in Table III. These parameters are derived from the dqz -axis current sweeping test. The prototype machine is designed to exhibit low core saturation, and it includes a cooling system that maintains a constant temperature throughout the experiment, ensuring stable machine parameters. SiC MOSFETs-based dual three-phase inverter applied to drive the DTP-PMSM. The control block diagram, shown in Fig. 7, is implemented on a custom FPGA development kit equipped with A/D conversion and an encoder acquisition circuit. During the experiment, the average switching frequency of proposed PWM technique is set to 15 kHz, the same as the comparative conventional PWM techniques. Therefore, the PWM carrier frequency is set to 15 kHz for DZIPWM, C6 Φ SVPWM24, and Seq1, 18 kHz for

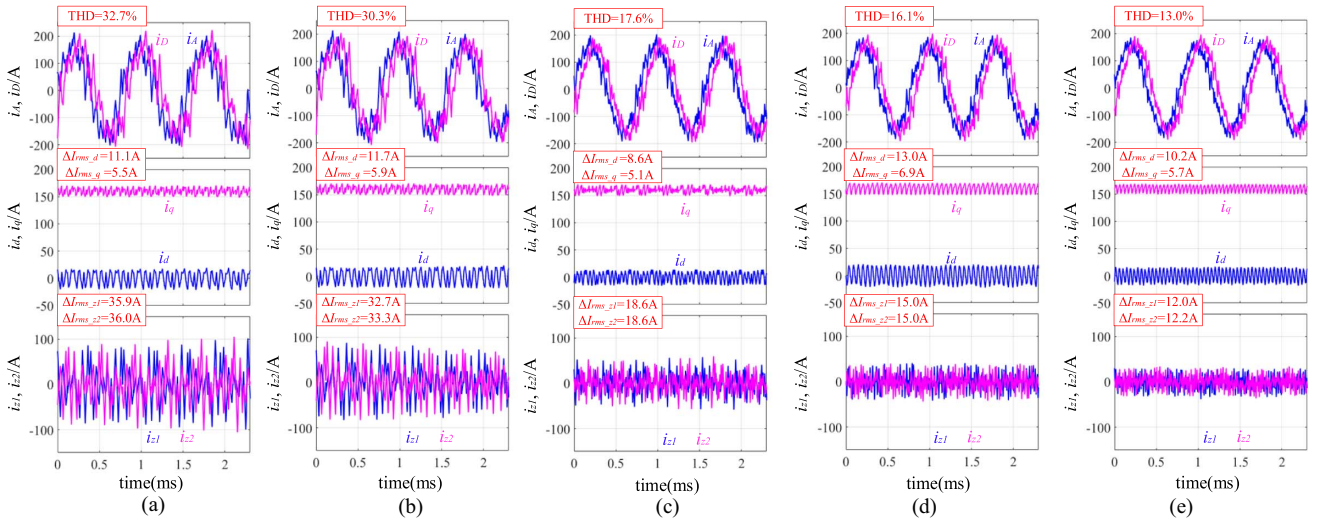


Fig. 11. Simulation results of A, D, phase currents, dq -axis currents, and z_{1z_2} -axis currents @ 16 000 r/Min, 120 Nm with different existing PWM techniques and the proposed PWM technique. (a) DZIPWM. (b) C6 ϕ SVPWM24. (c) D6 ϕ SVPWM24-B2. (d) D6 ϕ SVPWM12-B2. (e) Proposed PWM technique.

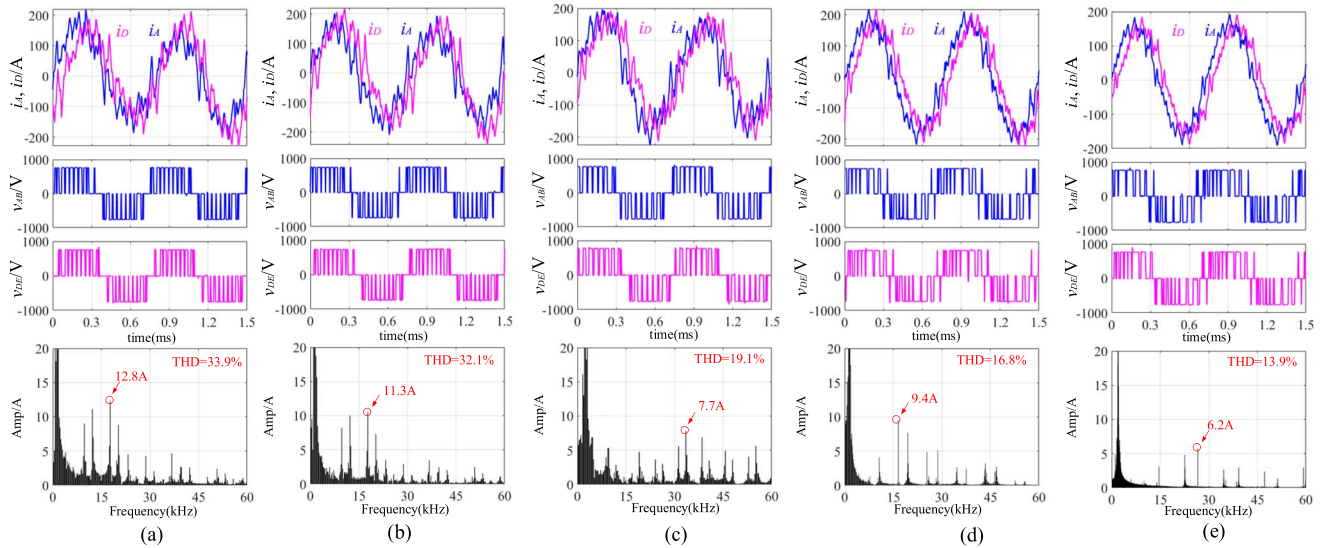


Fig. 12. Experimental results of A, D, phase currents, line-line voltages and spectrum of phase A currents @ 16000 r/Min, 120 Nm with different existing PWM techniques and the proposed PWM technique. (a) DZIPWM. (b) C6 ϕ SVPWM24. (c) D6 ϕ SVPWM24-B2. (d) D6 ϕ SVPWM12-B2. (e) Proposed PWM technique.

D6 ϕ SVPWM12-B2 and Seq2, 22.5 kHz for D6 ϕ SVPWM24-B2, Seq3, Seq4, and Seq5, ensuring switching losses about the same across different switching sequences. About 1 μ s dead-time is incorporated between the two complementary switches for each phase. The dc-link voltage is set to 750 V. Simulation is done using piecewise linear electrical circuit simulation (PLECS) with a DTP-PMSM model and ideal switching devices based on the machine parameters listed in Table III. All experiment waveforms are collected by TESTEC TTSI9010 differential probes, PEM CWTmini Rogowski current probes, Cleverscope CS548 oscilloscope, PPA5200 power analyzer. In compliance with IEEE Std 510–1983, the prototype and data acquisition equipment are remotely controlled. The collected data is subsequently processed and analyzed using MATLAB.

To demonstrate the improvement in current ripple performance through the proposed optimal PWM technique,

comparisons were conducted with existing PWM techniques via simulations and experiments under various conditions. Fig. 11 exemplifies this comparison, showcasing the current ripple performance at an operating condition of 16000 r/min and 120 Nm load, with the modulation amplitude ratio M set to 0.544 and the current parameters established at $i_d = 0$ A and $i_q = 160$ A. Compared with conventional PWM methods, the rms current ripple in the z_1z_2 -subspace is substantially reduced by the proposed PWM technique, particularly in the high modulation region where it significantly mitigates the majority of the current distortion. Additionally, the proposed method exhibits the lowest THD among the evaluated PWM techniques, validating the effectiveness of the proposed optimization objective in assessing the current distortion resulting from PWM effects. This evidence highlights the superior capability of the proposed PWM technique in improving current ripple performance.

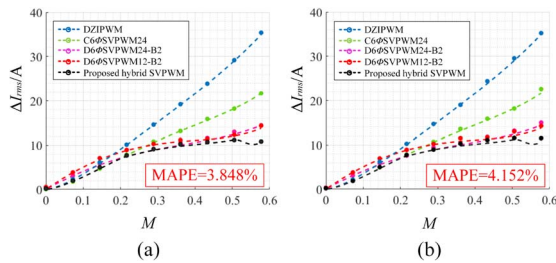


Fig. 13. Comparison of line-cycle rms current ripple of different PWM techniques versus M . (a) Simulations. (b) Experiments.

Fig. 12 displays the experimental results for phase A and D currents, alongside the line-to-line voltages v_{AB} and v_{DE} , including the spectrum analysis of phase currents up to 60 kHz. This comparison of different PWM techniques is conducted under conditions of 16000 r/min and a load of 120 Nm. The observed 30° phase shift between phase A , D currents and the line-to-line voltages v_{AB} , v_{DE} , confirms the fundamental operating principle of the dual three-phase PMSM. From the analysis presented in Fig. 12, it is evident that the proposed PWM technique achieves the lowest THD at 13.9% among the techniques compared, and it also exhibits the lowest peak sideband current harmonics near the switching frequency. Additionally, the PWM carrier frequency for the various PWM strategies can be seen in Fig. 12 through the center of the sideband current harmonics.

The analytical current ripple optimization objective is established as (7), and the line-cycle rms current ripple comparison between the proposed and existing PWM techniques is based on (14), as shown in Fig. 9. To validate the accuracy of the optimization objective and the analytical comparison, the line-cycle rms current ripple was also obtained from simulations and experiments, depicted in Fig. 13. Simulations and experiments were performed under varying speeds from 2000 to 16000 rpm with zero load. The modulation amplitude ratio for the dual three-phase PMSM was derived by analyzing the fundamental components of the line-to-line voltage. The comparison indicates a mean absolute percentage error (MAPE) of no more than 5% between the simulation/experimental results and the numerical calculations, demonstrating a close alignment of the simulated/experimented data points with the analytical predictions.

The proposed PWM optimal technique exhibits superior current ripple performance across the entire modulation region compared to existing PWM techniques. In the low modulation region, which is the optimal region of Seq1, the proposed PWM technique's performance aligns closely with that of C6 ϕ SVPWM24, the best among the existing techniques. As the modulation amplitude increases, the hybrid optimal regions incorporating C6 ϕ SVPWM24 and D6 ϕ SVPWM24-B2, D6 ϕ SVPWM12-B2 and D6 ϕ SVPWM24-B2 are selected. The proposed hybrid approach, considering both modulation amplitude ratio and electric angle, further reduces the current ripple compared to any individual technique. In the high modulation region, the application of the hybrid optimal regions of Seq4 and Seq5 demonstrates a significant improvement, by 23.6%, over the best existing technique at the maximum modulation point.

According to previous section analysis, the line-cycle rms current ripple performance can indicate the current distortion performance

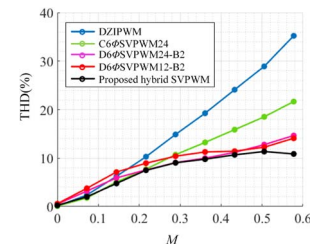


Fig. 14. Experimental comparison of THD of different PWM techniques versus M with the load of 120 Nm.

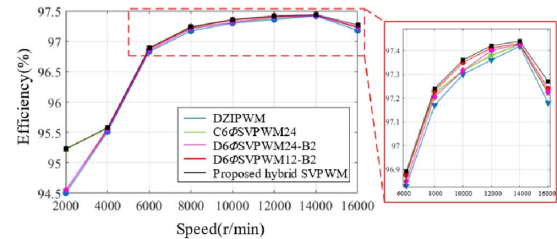


Fig. 15. Efficiency comparison of different PWM techniques under 16 000 r/Min, with 160 Nm torque.

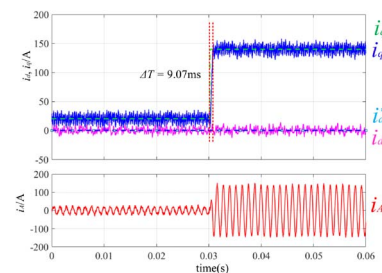


Fig. 16. Dynamic performance of the proposed PWM technique at 10 000 r/Min, step from 5% of full load to 50% of full load.

of PWM techniques. Fig. 14 displays the THD of phase A current under a load of 120 Nm across different modulation amplitudes. The comparison results for THD are consistent with those of the rms current ripple, with the proposed PWM technique showing the lowest THD throughout the entire modulation region.

Fig. 15 shows machine efficiencies across a speed range of 2000 to 16000 r/min while maintaining a constant torque of 120 Nm, comparing various PWM techniques. The proposed SVPWM strategy consistently delivers optimal efficiency across the modulation range, attributed to its current ripple suppression characteristics. For speeds below 6000 r/min, the efficiency of the proposed strategy nearly matches the peak efficiencies observed with C6 ϕ SVPWM24 and D6 ϕ SVPWM24-B2, given that the proposed PWM technique employs the same switching sequences. The divergence in efficiency becomes more pronounced above 6000 r/min, with a notable increment of 0.03% at 16 000 r/min. This enhancement is particularly evident when the proposed PWM technique uses switching sequences distinct from prior methodologies.

Fig. 16 shows the step response of proposed PWM technique as it manages a load transition from 5% to 50%. The figure captures the q -axis current, d -axis current, and phase A current, demonstrating how the system dynamically responds to changes. The

TABLE IV

RESPONSE TIME COMPARISON OF DIFFERENT PWM TECHNIQUES UNDER IDENTICAL PI PARAMETERS AND OPERATING CONDITIONS (REFER TO FIG. 16)

PWM Techniques	Dynamic Response Time
DZIPWM	9.13 ms
C6 ϕ SVPWM24	9.11 ms
D6 ϕ SVPWM24-B2	9.05 ms
D6 ϕ SVPWM12-B2	9.08 ms
Proposed PWM technique	9.07 ms

behavior of these responses is predominantly given by the PI settings within the current loop, underscoring the importance of control parameters in dynamic performance. To ensure a robust evaluation, other existing PWM techniques were subjected to the same operational conditions as shown in Fig. 16, with the settling times recorded in Table IV. Analysis reveals that with consistent PI parameters across all tested PWM techniques, the difference in response times is less than 1%. This indicates that the proposed PWM technique, despite applying various switching sequences for different modulation points, does not adversely affect the dynamic performance of the drive system compared to conventional fixed switching sequence PWM techniques.

VI. CONCLUSION

In this article, a PWM optimization strategy has been presented for dual three-phase PMSM. This strategy fully considers all potential switching sequences and provides a fair evaluation of their current ripple performance. Through this analysis, an optimal hybrid SVPWM strategy is proposed, which selects the switching sequences with best current performance for each (M, θ) numerically. The optimal region of different switching sequences is delineated by considering the variation of machine parameters. A carrier-based approach with dead-time compensation is proposed to simplify the PWM generation. Compared with traditional PWM techniques or the independent optimal switching sequences, this proposed strategy exhibits overall current ripple performance improvement exceed 20%, as substantiated by analytical, simulation, and experimental data. An increase in machine efficiency is also observed, stemming from the improved current ripple performance.

REFERENCES

- [1] F. Barrero and M. J. Duran, "Recent advances in the design, modeling, and control of multiphase machines—part I," *IEEE Trans. Ind. Electron.*, vol. 63, no. 1, pp. 449–458, Jan. 2016.
- [2] X. Wang, et al., "Torque ripple reduction in sectorized multi three-phase machines based on PWM carrier phase shift," *IEEE Trans. Ind. Electron.*, vol. 67, no. 6, pp. 4315–4325, Jun. 2020.
- [3] B. Zheng, J. Zou, B. Li, M. Tang, Y. Xu, and P. Zanchetta, "Analysis and fault-tolerant control for dual-three-phase PMSM based on virtual healthy model," *IEEE Trans. Power. Electron.*, vol. 37, no. 12, pp. 15411–15424, Dec. 2022.
- [4] D. Hadiouche, H. Razik, and A. Rezzoug, "On the modeling and design of dual-stator windings to minimize circulating harmonic currents for VSI fed AC machines," *IEEE Trans. Ind. Appl.*, vol. 40, no. 2, pp. 506–515, Mar./Apr. 2004.
- [5] Y. Zhao and T. A. Lipo, "Space vector PWM control of dual three-phase induction machine using vector space decomposition," *IEEE Trans. Ind. Appl.*, vol. 31, no. 5, pp. 1100–1109, Sep./Oct. 1995.
- [6] N. G. Marmolejo and M. Doppelbauer, "Influence of interleaved converters on iron losses in dual three-phase permanent magnet machines," in *Proc. 10th Int. Conf. Power Electron. Mach. Drives (PEMD)*, 2020, pp. 765–770. doi: 10.1049/icp.2021.0955.
- [7] Y. Miyama, M. Ishizuka, H. Komatani, and K. Akatsu, "Vibration reduction by applying carrier phase-shift PWM on dual three-phase winding permanent magnet synchronous motor," *IEEE Trans. Ind. Appl.*, vol. 54, no. 6, pp. 5998–6004, Nov./Dec. 2018.
- [8] Y. Hu, Z. Q. Zhu, and M. Odavic, "Comparison of two-individual current control and vector space decomposition control for dual three-phase PMSM," *IEEE Trans. Ind. Appl.*, vol. 53, no. 5, pp. 4483–4492, Sep./Oct. 2017.
- [9] L. Yan et al., "Suppression of major current harmonics for dual three-phase PMSMs by virtual multi three-phase systems," *IEEE Trans. Ind. Electron.*, vol. 69, no. 6, pp. 5478–5490, Jun. 2022.
- [10] M. Hu, W. Hua, W. Huang, and J. Meng, "Digital current control of an asymmetrical dual three-phase flux-switching permanent magnet machine," *IEEE Trans. Ind. Electron.*, vol. 67, no. 6, pp. 4281–4291, Jun. 2020.
- [11] Y. Hu, Z.-Q. Zhu, and K. Liu, "Current control for dual three-phase permanent magnet synchronous motors accounting for current unbalance and harmonics," *IEEE J. Emerg. Sel. Topics Power Electron.*, vol. 2, no. 2, pp. 272–284, Jun. 2014, doi: 10.1109/JESTPE.2014.2299240.
- [12] H. S. Che, E. Levi, M. Jones, W.-P. Hew, and N. A. Rahim, "Current control methods for an asymmetrical six-phase induction motor drive," *IEEE Trans. Power. Electron.*, vol. 29, no. 1, pp. 407–417, Jan. 2014.
- [13] J. Karttunen, S. Kallio, P. Peltoniemi, and P. Silventoinen, "Current harmonic compensation in dual three-phase PMSMs using a disturbance observer," *IEEE Trans. Ind. Electron.*, vol. 63, no. 1, pp. 583–594, Jan. 2016.
- [14] Y. Xu, B. Zheng, G. Wang, H. Yan, and J. Zou, "Current harmonic suppression in dual three-phase permanent magnet synchronous machine with extended state observer," *IEEE Trans. Power. Electron.*, vol. 35, no. 11, pp. 12166–12180, Nov. 2020.
- [15] P. R. Rakesh and G. Narayanan, "Analysis of sine-triangle and zero-sequence injection modulation schemes for split-phase induction motor drive," *IET Power Electron.*, vol. 9, no. 2, pp. 344–355, Feb. 2016. doi: 10.1049/iet-pel.2015.0066.
- [16] R. Bojoi, M. Lazzari, F. Profumo, and A. Tenconi, "Digital field-oriented control for dual three-phase induction motor drives," *IEEE Trans. Ind. Appl.*, vol. 39, no. 3, pp. 752–760, May 2003.
- [17] J. Prieto, E. Levi, F. Barrero, and S. Toral, "Output current ripple analysis for asymmetrical six-phase drives using double zero-sequence injection PWM," in *Proc. 37th Annu. Conf. IEEE Ind. Electron. Soc. (IECON)*, pp. 3692–3697, Nov. 2011, doi: 10.1109/IECON.2011.6119909.
- [18] D. Hadiouche, L. Baghli, and A. Rezzoug, "Space-vector PWM techniques for dual three-phase AC machine: Analysis, performance evaluation, and DSP implementation," *IEEE Trans. Ind. Appl.*, vol. 42, no. 4, pp. 1112–1122, Jul./Aug. 2006.
- [19] K. Marouani, L. Baghli, D. Hadiouche, A. Kheloui, and A. Rezzoug, "A new PWM strategy based on a 24-sector vector space decomposition for a six-phase VSI-fed dual stator induction motor," *IEEE Trans. Ind. Electron.*, vol. 55, no. 5, pp. 1910–1920, May 2008.
- [20] W. Kun, Y. Xiaojie, W. Chenchen, and Z. Minglei, "An equivalent dual three-phase SVPWM realization of the modified 24-sector SVPWM strategy for asymmetrical dual stator induction machine," in *Proc. IEEE Energy Convers. Congr. Expo. (ECCE)*, Sep. 2016, pp. 1–7, doi: 10.1109/ECCE.2016.7854842.
- [21] C. Zhou, G. Yang, and J. Su, "PWM strategy with minimum harmonic distortion for dual three-phase permanent-magnet synchronous motor drives operating in the overmodulation region," *IEEE Trans. Power Electron.*, vol. 31, no. 2, pp. 1367–1380, Feb. 2016.
- [22] C. Wang, K. Wang, and X. You, "Research on synchronized SVPWM strategies under low switching frequency for six-phase VSI-fed asymmetrical dual stator induction machine," *IEEE Trans. Ind. Electron.*, vol. 63, no. 11, pp. 6767–6776, Nov. 2016.
- [23] L. Wu et al., "Strategy of synchronized SVPWM for dual three-phase machines in full modulation range," *IEEE Trans. Power Electron.*, vol. 37, no. 3, pp. 3272–3282, Mar. 2022.
- [24] K. Cui et al., "Comprehensive investigation of space-vector PWM including novel switching sequences for dual three-phase motor drives," *IEEE Trans. Transport. Electrification.*, vol. 9, no. 1, pp. 1350–1362, Mar. 2023.
- [25] D. Ye et al., "Variable switching sequence PWM strategy of dual three-phase machine drive for high-frequency current harmonic suppression," *IEEE Trans. Power Electron.*, vol. 35, no. 5, pp. 4984–4995, May 2020.
- [26] S. Paul and K. Basu, "Linear PWM techniques of asymmetrical six-phase machine with optimal current ripple performance," *IEEE Trans. Ind. Electron.*, vol. 70, no. 2, pp. 1298–1309, Feb. 2023.



Sunbo Wang received the B.S. degree in electrical engineering from Beijing Institute of Technology, Beijing, China, in 2020. He is currently working toward the Ph.D. degree in electronic engineering with the Power Electronics, Machines and Control Group, University of Nottingham, Nottingham, U.K.

His research interests include control strategy of PM machines and multiphase machines, high efficiency high speed ac motor drives, and pulse-width-modulation strategies.



Marco Rivera (Senior Member, IEEE) received the B.Sc. degree in electronic civil engineering and the M.Sc. degree in electrical engineering from the Universidad de Concepción, Concepción, Chile, in 2007, and 2008, respectively, and the Ph.D. degree in electronic engineering from the Universidad Técnica Federico Santa María, Valparaíso, Chile, in 2011.

Through the last years, he has been a Visiting Professor with several international universities. He has directed and participated in several projects

financed by the National Fund for Scientific and Technological Development (Fondo Nacional de Desarrollo Científico y Tecnológico, FONDECYT), the Chilean National Agency for Research and Development (Agencia Nacional de Investigación y Desarrollo, ANID), and the Paraguayan Program for the Development of Science and Technology (Proyecto Paraguayo para el Desarrollo de la Ciencia y Tecnología, PROCENCIA), among others. He has been the responsible researcher of basal financed projects whose objective is to enhance, through substantial and long-term financing, Chile's economic development through excellence and applied research. He is the Director of the Laboratory of Energy Conversion and Power Electronics (Laboratorio de Conversión de Energías y Electrónica de Potencia, LCEEP) with the Universidad de Talca, Talca, Chile. He was a Full Professor with the Department of Electrical Engineering, the Universidad de Talca. Since 2023, he joined the Power Electronics, Machines and Control (PEMC) Research Institute of the University of Nottingham, Nottingham, U.K., as a Professor. His research interests include the power electronics, renewable energies, advanced control of power converters, microgrids, and among others. He has published more than 520 academic publications in leading international conferences and journals.

Dr. Rivera was awarded the "Premio Tesis de Doctorado Academia Chilena de Ciencias 2012", for the best Ph.D. Thesis developed in 2011 for national and foreign students in any exact or natural sciences program, that is member of the Academia Chilena de Ciencias, Chile.



Dmitry Golovanov received the Ph.D. degree in superconducting electrical machines from Moscow Aviation Institute, Moscow, Russia, in 2011.

Currently, he is an Engineer with Williams Advanced Engineering (WAE), Oxfordshire, U.K. He has experience of working in academia and industry in the field of electrical machines design as well as in the field of Li-ion batteries development. His research interests include designing electrical machines and drives as well as motor control

system development for aerospace and automotive industry.



Jonathan Blissett received the M.Eng. and Ph.D. degrees in electrical engineering from the University of Nottingham, Nottingham, U.K., in 2014 and 2018 respectively.

Currently, he is an Engineer with Williams Advanced Engineering (WAE), Oxfordshire, U.K. His current role covers varied interests combining system-based design powertrain optimization with electromagnetic design and control of electrical machines. His research interests include modeling of electric motorcycles and electrical machines for

motorsport applications.



Jonathan Moran received the B.Eng. degree in electrical and electronic engineering from the University of Nottingham, Nottingham, U.K., in 2017.

Moving straight into the research and development area of the EV traction motor drives industry, he has worked on a variety of power electronics projects centred around cutting edge lightweight and highly efficient power converters. Currently, he is an Engineer with Williams Advanced Engineering (WAE), Oxfordshire,

U.K. His research interests include anything related to improving and delivering EV powertrain performance.



Paul Davison received the Ph.D. degree in nonlinear aircraft dynamics and control from the University of Bristol, Bristol, U.K., in 2003.

He subsequently spent nine years working trackside in Formula one before transferring to the electric racing series. Currently, he is the Head of Control Performance, working on control system and powertrain development in the racing domain.



G. Ramtharan received the B.Eng. (Hons) degree in electrical and electronic engineering from the University of Peradeniya, Peradeniya, Sri Lanka, in 2002 and the Ph.D. degree from the University of Manchester, Manchester, U.K., in 2008.

Currently, he holds the position of Chief Engineer in electric powertrains. His research interest includes multi-MW powertrains for wind turbines. He then spent seven years on various powertrains for large wind turbines before making

a transition to the electric racing series.



Chris Gerada (Senior Member, IEEE) received the Ph.D. degree in numerical modeling of electrical machines from the University of Nottingham, Nottingham, U.K., in 2005.

He was a Researcher in high-performance electrical drives and the design and modeling of electromagnetic actuators for aerospace application with the University of Nottingham. In 2008, he was a Lecturer in electrical machines, in 2011, an Associate Professor, and in 2013, a Professor with the University of Nottingham. His

research interest includes the design and modeling of high-performance electric drives and machines.



Patrick Wheeler (Fellow, IEEE) received the B.Eng. and Ph.D. degrees in electrical engineering for his work on matrix converters from the University of Bristol, Bristol, U.K., in 1990 and 1994, respectively.

In 1993, he moved to the University of Nottingham and worked as a Research Assistant with the Department of Electrical and Electronic Engineering. In 1996, he became a Lecturer with Power Electronics, Machines and Control Group, University of Nottingham, Nottingham,

U.K. Since 2008, he has been a Full Professor with the same research group. Currently, he is the Global Engagement Director with the Faculty of Engineering, the Head with the Power Electronics, Machines and Control Research Group, and the Director with the University of Nottingham's Institute of Aerospace Technology. He was the Head with the Department of Electrical and Electronic Engineering, University of Nottingham, from 2015 to 2018.